Theses and Dissertations   Student Graduate Works

3-11-2011

Nuclear Weapon Yield Determination through Nano Indentation of Thermally Degraded Automobile Paint

Michael J. Richards

Follow this and additional works at: https://scholar.afit.edu/etd

Part of the Nuclear Commons

NUCLEAR WEAPON YIELD DETERMINATION THROUGH

NANO INDENTATION OF THERMALLY

DEGRADED AUTOMOBILE PAINT

THESIS

Michael Joseph Richards, Captain, USAF

AFIT/GNE/ENP/11-M17

DEPARTMENT OF THE AIR FORCE

AIR UNIVERSITY

AIR FORCE INSTITUTE OF TECHNOLOGY

Wright-Patterson Air Force Base, Ohio

APPROVED FOR PUBLIC RELEASE; DISTRIBUTION UNLIMITED

AFIT/GNE/ENP/11-M17

NUCLEAR WEAPON YIELD DETERMINATION THROUGH

NANO INDENATION OF THERMALLY

DEGRADED AUTOMOBILE PAINT

THESIS

Presented to the Faculty

Department of Engineering Physics

Graduate School of Engineering and Management

Air Force Institute of Technology

Air University

Air Education and Training Command

In Partial Fulfillment of the Requirements for the

Degree of Master of Science in Nuclear Engineering

Michael J. Richards, BS

Captain, USAF

March 2011
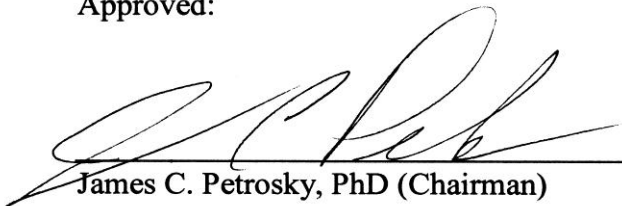
AFIT/GNE/ENP/11-M17

NUCLEAR WEAPON YIELD DETERMINATION THROUGH

NANO INDENTATION OF THERMALLY

DEGRADEDAUTOMOBILE PAINT

Michael J. Richards, BS

Captain, USAF

Approved:

_____
James C. Petrosky, PhD (Chairman)

_____
Larry W. Burggraf, PhD (Member)

_____
Shankar Mall, PhD (Member)

4/Mar-11
Date

3 Mar 2011
Date

3/7/2011
Date

Abstract

The national level response to a nuclear attack on an American city would depend heavily on the information that can be determined about the weapon immediately after the event. A vital piece of that information is the yield of the weapon. Current methods for determining yield suffer from one or more of wide confidence intervals, long event-to-analysis lag time, and insufficient sensors. A proposed method for determining yield that has the potential to overcome these limitations relies on the change in automobile paint caused by the thermal pulse of the weapon.

This work investigated the suitability of automotive clearcoat as a nuclear weapon yield sensor, using the change in elastic modulus as the primary metric. The AFIT Xenon Thermal Simulator (AXTS) was used to simulate a nuclear thermal pulse. The elastic modulus of the clearcoat was measured using a nano indenter. During this research the power density of the AXTS beam was increased from 44.7 to 63.7 W/cm^2. The morphological steps through which automobile paint proceeds as it thermally degrades were identified and correlated with temperatures. A computer model was created and used to ensure that the paint's time-temperature response to the AXTS pulse was comparable to that of a replicate nuclear thermal pulse.

Clearcoat's physical properties exhibit a low sensitivity to incident thermal energy. Variability among these properties remains essentially unchanged by exposure to the thermal pulse. A weak correlation between change in elastic modulus and exposure time was identified. A similarly weak correlation between exposure time and each of

load on sample, harmonic stiffness, and hardness was also identified. It was concluded

that these correlation were too weak to be used for post-detonation forensics.

Acknowledgements

I would like to acknowledge the many people who have helped me in this process and express my gratitude for the sacrifices they've made for me. First, Dr. Petrosky has been a fantastic advisor. Ever the teacher, he always seemed to ask the questions that pointed me in the right direction. My committee members, Drs. Burggraf and Mall, similarly provided invaluable guidance as I struggled through the vicissitudes of research. Lt Col McClory regularly expressed interest in my progress and encouraged me. Eric Taylor was extremely helpful and provided excellent service every time I needed him. Without all these people and many more, I would not have been able to finish this work. Thank you.

Michael J. Richards

Table of Contents

List of Figures

List of Tables

List of Symbols and Acronyms

AFIT xenon thermal simulator (AXTS)

Continuous stiffness measurements (CSM)

Kiloton (kT)

Pigment volume concentration (PVC)

Scanning electron microscope (SEM)

Ultra violet (UV)

NUCLEAR WEAPON YIELD DETERMINATION THROUGH

NANO INDENTATION OF THERMALLY DEGRADED AUTOMOBILE PAINT

I. Introduction

1.1 Problem Statement

The detonation of a nuclear weapon in an American city by a terrorist organization would have severe consequences. The extent of those consequences would depend largely on the ability of nuclear forensics teams to piece together the details of what happened. National level response would depend heavily on the information from those teams. An accurate estimate of the weapon yield is important for forensics and consequence management. A yield estimate is required for the techniques used in attribution analysis, for determining pre-detonation weapon characteristics, and for many of the models used in predicting fallout patterns and dose estimates. Current methods for determining yield suffer from one or more of wide confidence intervals, long event-to-analysis lag time, and insufficient sensors. A method is needed that can provide a yield estimate that is both accurate and rapid.

1.2 Background

A proposed method for determining yield that has the potential for being both accurate and rapid uses the degradation of automobile paint caused by the thermal pulse of a nuclear weapon (Sjoden et al., 2009). This method has several advantages over other techniques, including ubiquitous available sensors, knowledge of pre-event conditions,

insignificant effect of removing the samples, and substantial measurements from surface weapons testing. Because in any single nuclear weapon event only one side of an automobile will face the weapon, the opposite side will be in the "shadow" of the thermal pulse. Measurements of the "shadow" side can be compared to measurements of the side exposed to the thermal pulse, and the differences in the properties of the two sides can be used to determine the yield of the weapon.

Experimental evaluation of this potential method was initiated previously (Koehl, 2009). The AFIT Xenon Thermal Simulator (AXTS) was assembled and it was shown that mass loss and degradation could be correlated to weapon yield (Koehl, 2009). In the work of (Bauer, 2010), the thermal energy flux of the AXTS was increased, the spectral output and flux profile of the AXTS were characterized, and mass loss of automobile paint with simulated nuclear weapon yield was correlated. In a concurrent and parallel computational effort, (Stachitas, 2009) began modeling the effect of an urban street canyon on the transport of thermal energy from a nuclear weapon and (Mock, 2010) modeled the mass loss response of automobile paint to thermal energy. This work focuses on changes in elastic modulus of automobile paint due to thermal degradation in order to continue the evaluation of the proposed forensic technique.

1.3 Hypothesis

Differences between the elastic modulus, as measured by nano indentation, of automobile paint samples subject to thermal irradiation from a simulated nuclear weapon and unirradiated samples will exist such that a model relating those differences to the power and duration of exposure can be developed.

1.4 Conclusion

This research demonstrated that there is a weak correlation between the average modulus measured from 9 to 10 µm beneath the surface of black automobile paint and the length of exposure to a thermal pulse. This correlation can be described with the following function,

$$\Delta M = -0.365 + 0.867t,$$

where ΔM is the change in elastic modulus, and t is the duration of irradiation. The R^2 value for this correlation equation's fit to the measured data is 0.4400. While this is evidence of a correlation, it is insufficiently precise to be used as a stand-alone forensics tool.

In addition to average modulus, equations of best fit were determined for the curves of load on sample, modulus, harmonic stiffness, and hardness as functions of depth. The parameters of these equations were correlated with exposure time. These correlations were also found to be too weak for forensics use.

1.5 Paper Organization

This thesis is presented in the following chapters: Chapter 2 – Theory; Chapter 3 – Experiment; Chapter 4 – Results; Chapter 5 – Analysis, and Chapter 6 – Conclusions. Chapter 2 provides a basic discussion of the germane elements of nuclear explosions, modern automobile paint, and nano indentation measurements. Chapter 3 discusses the equipment used, method of preparing the samples, and procedures used in conducting the experiments. Chapter 4 presents the results and the method used for conditioning the results for analysis. Chapter 5 provides an analysis of the results obtained. Chapter 6

concludes the discussion of this research as well as makes recommendations for future research to be pursued.

II. Theory

2.1 Nuclear Weapons

Energy from a nuclear weapon takes on many forms. The energy is initially

released as kinetic energy of particles, gamma rays, and neutrinos. Within a short time,

most of this energy is converted into x-rays, which are largely and subsequently down-

scattered to lower energy photons in the visual and IR range. As an example, Figure 1

shows the spectral energy distribution of the thermal pulse of a 1 kT surface burst at a

distance of over 15 km. The left shaded portions denote the ultra-violet (UV) region; the

central portions, the visible region; and the right shaded portions, the infrared region. UV

and visible light photons, which travel greater distances through air than x-rays, are

primarily responsible for the thermal pulse associated with a nuclear weapon. A portion

of the weapon's energy is also converted into a blast wave.
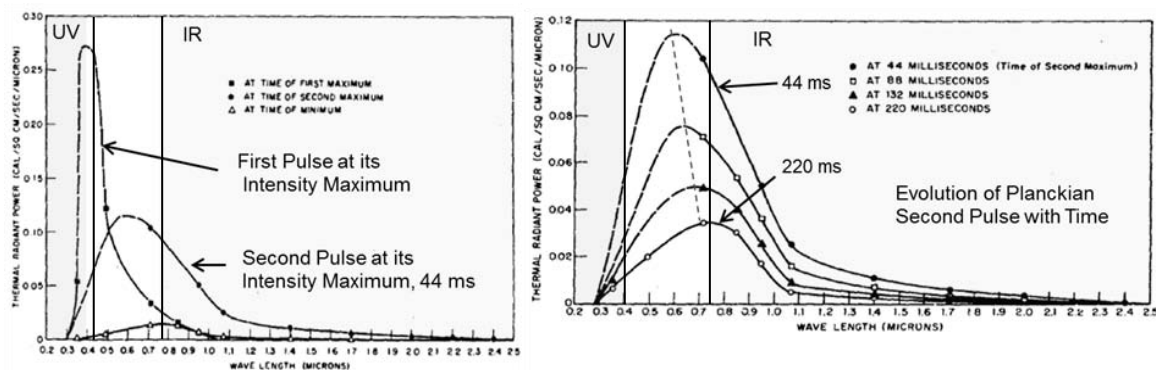
Figure 1. Reproductions of Figures 3.1 and 3.2 from (Plum et al., 1958): average intensity
measurements from a 1 kT nuclear device

The strength of the blast wave and the thermal pulse depend on a number of

factors including the density of the air in which the weapon was detonated, the distance

of the weapon from the ground, the surrounding environment, whether open air or urban setting, and the surface material.

The thermal pulse and blast wave are of primary importance in this research. In order for the proposed technique for determining yield to be of use, there must be a location within the affected region where the blast wave is weakened such that it will not displace an automobile from its initial location and where the effects of the thermal pulse on automobile paint are detectable. Using nuclear weapon test data (Bauer, 2010) and (Koehl, 2009) showed that such a region exists, and (Bauer, 2010) showed it is possible to simulate the thermal pulse within this region using the AXTS. The test data was collected in essentially open atmosphere and thus has limits to its applicability in urban settings. (Stachitas, 2009) demonstrated that an urban street canyon has the effect of increasing the intensity of a thermal pulse by approximately 25%. This increase in intensity effectively extends the distance from ground zero at which one might find a thermally induced change in automobile paint properties.

2.2 Automobile Paint

Automobiles are painted for two primary reasons. First, paint protects the body of the vehicle from corrosion. Second, paint makes the vehicle's appearance more attractive. Automobile paints have gone from a simple primer, top coat system in the early 1900's to a modern multi-layer, multi-material system. In modern automobiles a typical paint system consists of a zinc phosphate layer, an electrocoat primer, a surfacer, a basecoat, and a clearcoat (Lambourne, 1999). Figure 2 is an image of a paint sample that has been sectioned and measured using an optical microscope. The different layers

of the paint system are shown. The role of each layer is discussed in the following
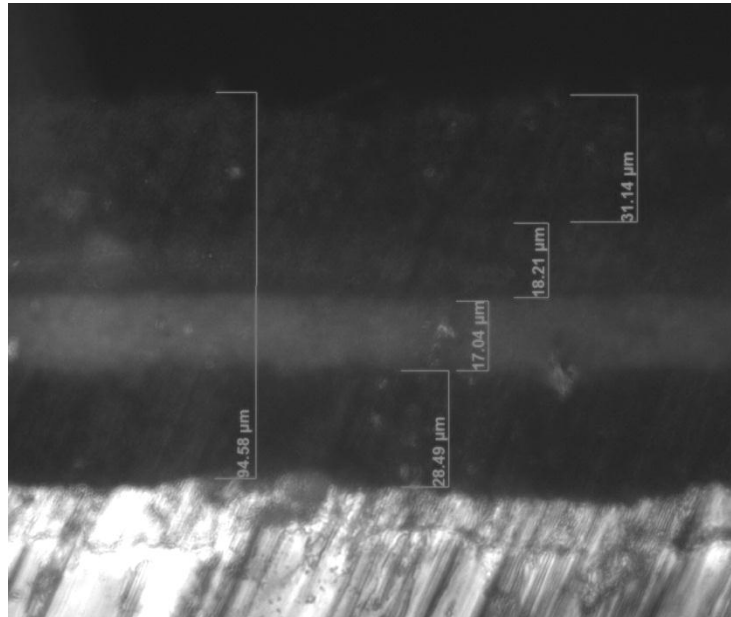
sections.

Figure 2. Optical microscope image of a sectioned paint sample

2.2.1 Zinc Phosphate Layer

The zinc phosphate layer is included in the system to prevent corrosion of the

steel substrate and to provide an inert surface to which subsequent layers can bind.

Before this layer can be added, the steel must be cleaned to remove accumulated oxides

and manufacturing oil residues remaining from the forming process. Once clean, the

steel is submerged in a zinc phosphate, phosphoric acid solution. The acid reacts with the

iron in the steel and leads to the formation of zinc phosphate crystals on the steel surface.

These crystals grow until they cover the entire surface of the steel, and the reactions cease

(Lambourne, 1999).

2.2.2 Electrocoat Primer

Electrocoat primer is a modern version of the basic primer layer that has been used in paint systems for many years. This layer's primary function is to act as a corrosion inhibiter. The primer in aqueous solution consists of an epoxy/amine resin system neutralized with acids. By electrically charging the steel, the cationic resins of the primer adhere to the surface of the vehicle body (Lambourne, 1999).

2.2.3 Surfacer (Filler)

The next layer in the system is referred to by a number of different names. Most names, including surfacer, filler, middle coat, and primer convey the function of the layer. When less complicated paint systems were used, the primer filled the role of surfacer. As each layer of paint became more specialized, however, a surfacer layer separate from the primer was required. The surfacer of modern automobile paint provides a smooth, even surface upon which to apply the pigment layer of the paint system. It essentially fills the holes, pits, and divots remaining in the surface of the electrocoat primer. Surfacers are typically composed of polyesters and 15-20% pigment volume concentration (PVC) (Lambourne, 1999).

2.2.4 Basecoat and Clearcoat

The two remaining layers in modern automobile paint systems are the basecoat and clearcoat. The basecoat provides color and the clearcoat provides gloss and protection. Basecoats are typically composed of a thermosetting acrylic polymer reacted with a melamine resin. They contain a high PVC as required to provide the color. The clearcoat consists of a thermosetting acrylic reacted with a melamine resin and no

pigment. Figure 3 provides a nominal illustration of the typical layers used in modern automobile paint systems.

Clearcoat (40-50 microns)
Basecoat (20 microns)
Surfacer/Filler (35-40 microns)
Electrocoat (18-25 microns)
Zinc Phosphate layer
Metal (Steel Substrate)

Figure 3. Nominal automotive coating layers (Adamsons, 2002)

2.3 Nano Indentation

Nano indentation is a form of instrumented indentation measurement that has become a mainstay in determining material properties of single layer coatings (Poilane, 1999), multi-layer coatings (Drzal et al., 2005), and composite materials (Delobellea et al., 2002). Measurements are made by depressing an indenter tip into the surface of a material and then removing it. During the process the load on and the displacement of the tip are measured. A nominal graph resulting from an indentation measurement is provided in Figure 4.

Using the stiffness, S, which is determined by the slope of the curve at the point of unloading, an effective elastic modulus, E_{eff}, can be determined by

$$S = \beta \frac{2}{\sqrt{\pi}} E_{eff} \sqrt{A}$$
,

where β is a geometric constant (1.034 for Berkovich type indenter) and A is the projected area of the indentation and is a function of displacement into the surface, h. E_{eff} is a composite of the sample modulus, E, and the system modulus, E_i. E can be determined from E_{eff} by
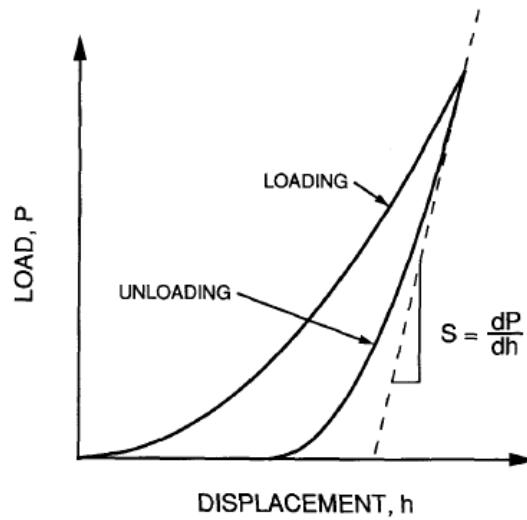
Figure 4. Nominal graph of load vs. displacement from a nano indentation measurement (Oliver, 2003)

$$\frac{1}{E_{eff}} = \frac{1-v^2}{E} + \frac{1-v_i^2}{E_i}$$

where v_i and v are Poisson's ratio for the system and the sample respectively.

Continuous stiffness measurements (CSM) can be performed using these same principles. By oscillating the indenter tip, the elastic modulus of the sample as a function of depth can be determined. The nano indenter measures the phase difference, φ, between the driving signal and the indenter tip response and uses this, instead of the slope of the loading curve at the point of unloading, to determine the harmonic stiffness, S, by

$$\tan\varphi = \frac{\omega D}{S + K_s - m\omega^2}$$

where ω is the driving frequency, D is a damping coefficient, m is the mass of the indenter tip, and K_s is the stiffness of the indenter shaft support springs (Fischer-Cripps, 2002). Figure 5 is an example of the results of a number of CSM acquisitions.
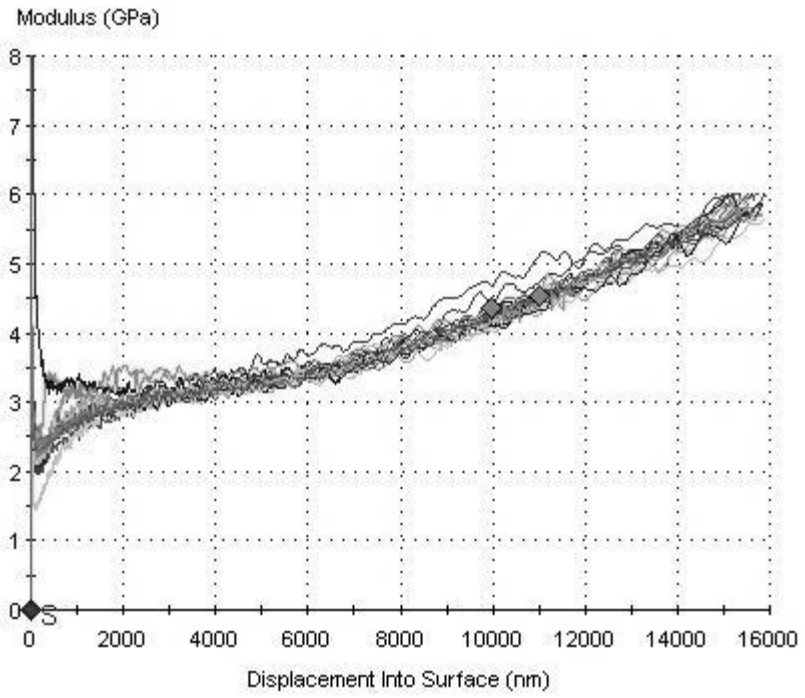
Figure 5. Nano indentation continuous stiffness measurement of a black paint sample

III. Experiment

This chapter discusses the experiments performed for this research. It begins with a discussion of the different pieces of equipment used and continues with a description of the samples. The evolution of the procedures used to conduct the experiments is also discussed. The chapter concludes with a discussion of the assumptions and limitations associated with this experiment.

3.1 Equipment

This section provides a brief overview of the equipment used in this research.

3.1.1 AFIT Xenon Thermal Simulator

The Newport Solar Simulator supplies the core of the AXTS, which is pictured in Figure 6. As assembled by (Koehl, 2009), the AXTS consisted of the solar simulator with associated shutter and power controllers, a 4 inch diameter, 200 mm focal length, fused silica lens, and position controllers and stages for the lens and sample. It was modified by (Bauer, 2010) to include a 2 inch, 150 mm fused silica lens. With this addition, the power output was increased from 13.8 to 44.8 W/cm^2. (Bauer, 2010) also measured the spectral output of the AXTS and compared it to that measured in Operation Teapot. As shown in Figure 7, the output of the AXTS falls within that of a real nuclear weapon. In the course of this research, the 150 mm lens was replaced with a 67.5 mm lens, and the lenses were repositioned. These changes increased the average measured power on the sample to 63.7 W/cm^2 and the peak power at the center of the beam to 81.3 W/cm^2.

Figure 6. AFIT Xenon Thermal Simulator
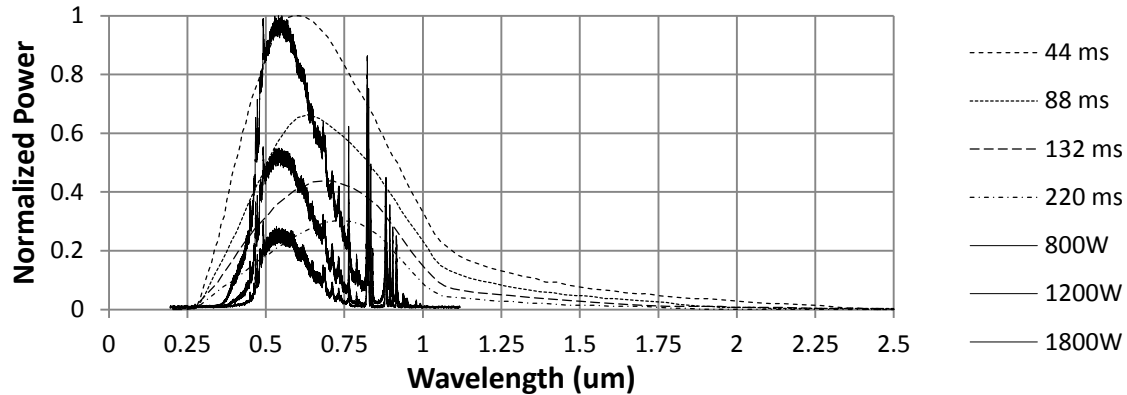
Figure 7. **Superposition of the spectral output of the AXTS at 800, 1200, and 1800 W (solid lines) over the spectral output at 4 different times after detonation of a test device used in Operation Teapot (dashed lines) (Plum, 1958)**

3.1.2 Nano Indenter

The Agilent G200 Nano Indenter XP, Figure 8, equipped with a Berkovich type indenter tip, allows for highly accurate measurements of load, displacement, and harmonic frequency. In addition, it boasts precise lateral control and a large working area which allows for multiple samples to be loaded at a single time. Specifications for the G200 can be found in Appendix A. Agilent Nano Indenter G200 Specifications.
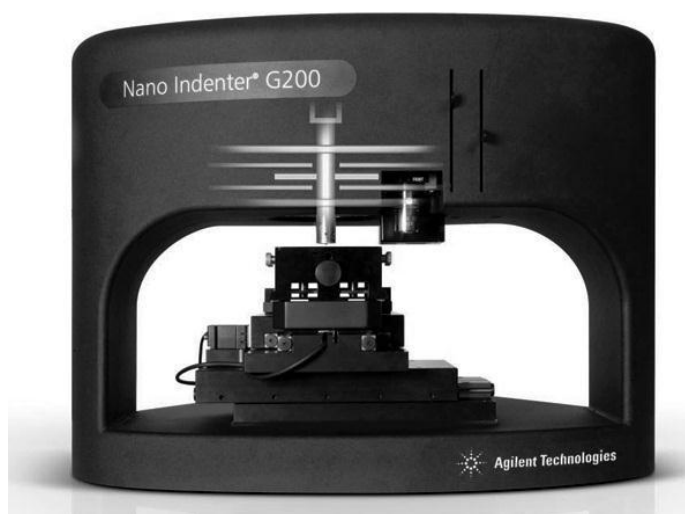
Figure 8. Agilent Nano Indenter G200

3.1.3 Microscopes

Two microscopes were used for evaluation of the morphological changes that occur during the thermal degradation of the paint. An optical microscope, the Zeiss Axio Imager.M2m (see Figure 9) and a scanning electron microscope (SEM), the Zeiss Evo LS10 (see Figure 10).

Figure 9. Zeiss Axio Imager.M2m

Figure 10. Zeiss Evo LS10 Scanning Electron Microscope

3.1.4 Thermal Camera

A FLIR ThermaCam PM 695 was used to measure the temperature response of

the paint samples to irradiation. Based on microbolometer technology, the PM695 has a

resolution of 320 x 240 pixels and detects from -40°C to 2000°C ±2%. See Appendix B.

FLIR PM695 Specifications for full specifications.

A microbolometer makes use of the fact that certain materials electrical resistivity changes as temperature changes. By selecting materials whose resistivity varies greatly with temperature, a sensitive device can be created. Vanadium oxide is currently the most widely used material because of its resistive sensitivity to temperature and its absorptivity of infrared radiation (Capper et al., 2001). Figure 11 is a drawing of a typical microbolometer cell.
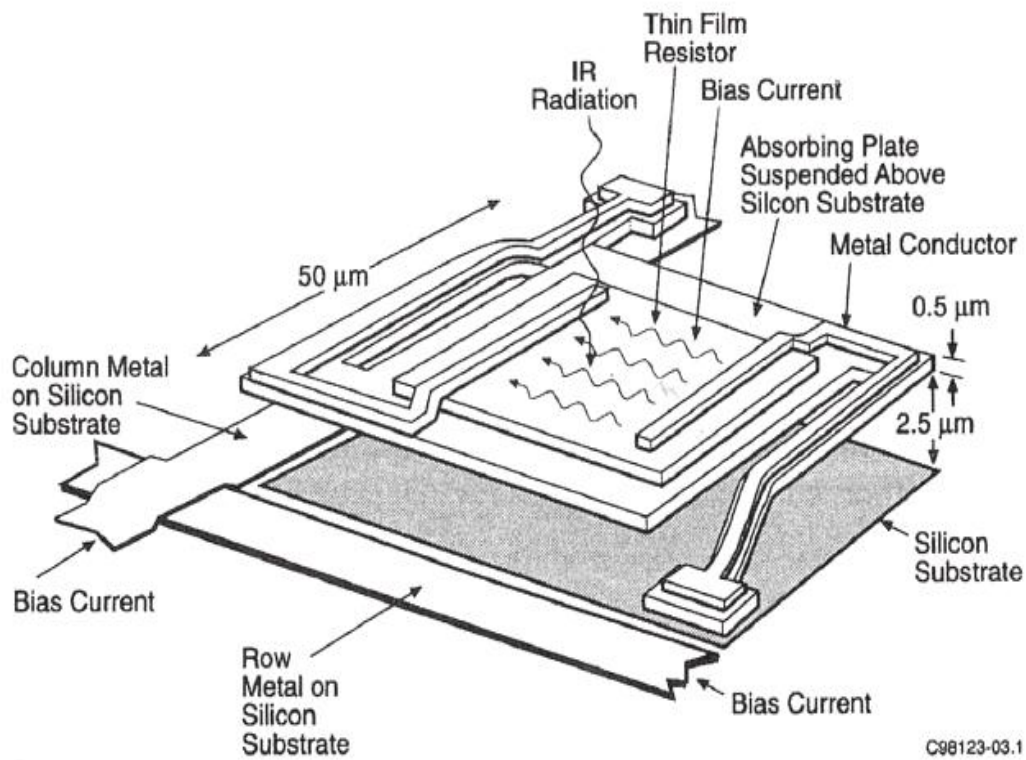
Figure 11. A typical microbolometer cell (Capper et al., 2001)

3.1.5 Power Detector

A Newport 2936-C power meter (see Figure 12) with an 818P-030-18HP thermopile was used to measure the power produced by the AXTS. Appendix C. Newport 818P-030-18HP Thermopile Specifications and Appendix D. Newport 2936-C Parameters contain the specifications and parameters that were used and also contain the response curve of the detector.

A thermopile is a set of thermocouples connected in series or parallel. By measuring the temperature gradient caused by incident radiation, the thermopile is able to calculate the incoming power. When used as an array, as the 818P is, a flux may be determined by dividing the total power detected by the array by the area exposed to the radiation.

Figure 12. Newport power meter

3.2 Samples

One half each of two identical car doors were painted a different color—red, blue, black, and white in accordance with Buick manufacturing specifications. This research

focused exclusively on black paint, and all results presented here are for black paint.

Circular samples, 1 cm in diameter, were cut using a water jet. Each sample was cleaned

according to cleaning method 1 as developed by (Bauer, 2010).

3.3 Evolution of the Experimental Procedure

3.3.1 Final Experimental Procedure

The final procedure used for the experiments is listed as follows. Each sample

was:

1. Cleaned in accordance with cleaning method 1, (Bauer, 2010),
2. Mounted on an SEM sample mounting pin,
3. Indented 25 times on the G200,
4. Mechanically removed from the pin,
5. Positioned on the sample holder,
6. Irradiated by the AXTS,
7. Remounted on the SEM sample mounting pin, and
8. Indented 25 times on the G200.

This procedure represents the culmination of a number of iterations and

associated decisions regarding the most effective method for conducting the experiment.

That evolution is presented in the following sections.

3.3.2 Sample Holders

Initially the AXTS was set up as described by (Bauer, 2010) with the exception of

the use of a modified mounting, positioning, and sample control system. This system

was built around the Pella SEM mounting pin, as shown in Figure 13.
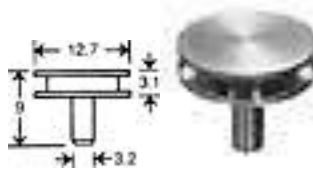
Figure 13. Pella SEM mounting pin, dimensions in mm

The system consisted of the Pella SEM mounting pins, a pin positioning post, which enabled repeatable positioning of the samples within the AXTS, and reusable nano indenter mounting pucks. Figure 14 shows the elements of the system with a paint sample mounted to the pin in the mounting puck and an empty pin in the post. The use of the mounting pins also aided in sample control by providing a surface on which to record the sample number of each of the individual paint samples. The primary benefit of the pins, and the system as a whole, was the ease with which the samples could be transferred from one device to another. Each sample was mounted to the pins with cyanoacrylate.
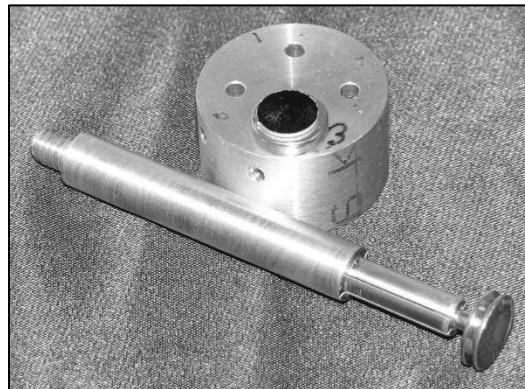
Figure 14. Reusable nano indenter mounting puck with pin and mounted paint sample and pin positioning post with pin

Upon initial testing, however, it was discovered that the paint samples did not attain temperatures as high as those observed by (Bauer, 2010). It was assumed that this

was a result of the change to the mounting technique—in particular that by using the SEM pins, a heat sink had been attached to the sample, providing a large thermal capacitance, thus lowering the maximum temperatures achieved. To test this theory, samples were mounted per (Bauer, 2010) and the tests were repeated. Again, the temperatures achieved were significantly lower, averaging about 33% less, than those observed by (Bauer, 2010), though they were higher than observed in those that had been mounted to the SEM pins. Because the presence of the SEM pins led to a significantly lower temperature, it was decided that the paint samples should not be mounted to the pins during the irradiation.

It was anticipated that high repeatability of the elastic modulus of the paint samples prior to irradiation would preclude the need for pre-irradiation indentations. This anticipation, however, turned out to be incorrect because of the surprisingly large variability in the pre-irradiated paint properties. This presented a problem in the need to mount the samples in order to indent them and then the need to remove the samples from the pins after the indentation to irradiate them. A number of methods for removing the samples from the pins were considered including chemically dissolving the cyanoacrylate, prying the sample free and mechanically shocking the sample free. Mechanically shocking was identified as the least damaging to the paint samples.

The decision to only irradiate un-mounted samples rendered the mounting post obsolete, and demanded a new method for holding the sample during irradiation. In the situation the experiment was attempting to simulate, a fairly uniform flux of energy would be incident on a portion of automobile body. The exposed auto body panel's primary methods of heat loss would be radiation and free convection on both the outside

and inside of the panel except where the body was joined to the frame,. Air flow on the inside of the panel would likely be obstructed by other components of the automobile, thus reducing the rate of heat transfer by free convection on the inside.

With this idea in mind, it was determined that the most expedient way to replicate these heat transfer mechanisms would be to have the sample held in place against an insulating material, while trying to avoid significant conductive heat loss to the insulation. This could be realized by reducing the contact area between the sample and the insulating material and by using the minimum force required to keep the sample in place. It was decided that using a piece of insulating, fibrous foam mounted to a magnet and held in place by a standard lens holder would satisfy those requirements. The fibrous surface of the foam provided a relatively small contact area, and the magnet provided just enough force on the sample to keep it from sliding off the mount from its own weight. A circle drawn on the insulating foam with a small notch for orientation enabled repeatable positioning of the samples. The sample holder is pictured in Figure 15.
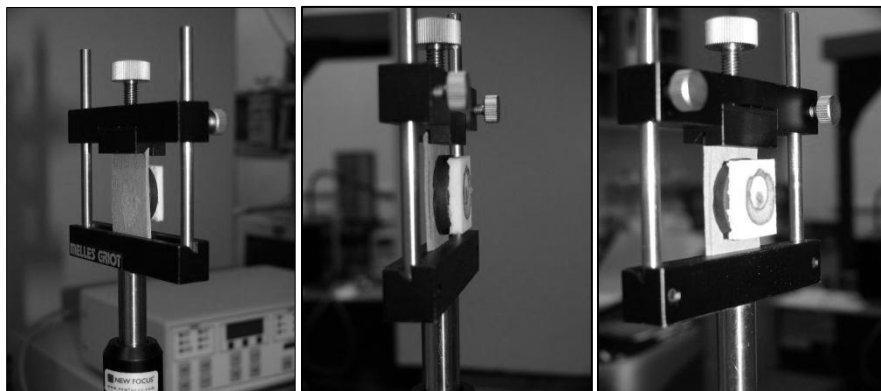
Figure 15. Redesigned sample holder featuring a magnet and insulating foam

3.3.3 AXTS Set-up

In consideration of the lower temperatures attained even when using the setup

from (Bauer, 2010), the question was raised whether the xenon bulb had degraded in

power output during its lifetime. When this research was started the bulb had been in

operation a total of 90 hours. By the end of this research is had surpassed 150 hours.

Power degradation with usage is a normal behavior for xenon bulbs, but they are

recommended to be replaced only after a total of 600 hours of operation (Newport, 2008).

The power output of the AXTS was measured with the Newport 818P-030-18HP

thermopile. This thermopile has a slow response time due to the filter placed over the

detector to prevent the detector from becoming saturated when measuring high power

levels. Because of the slow response, a method was developed to ensure that the steady

state power was measured and not part of the rise, overshoot, or fall experienced by the

detector as shown in Figure 16.

Figure 16. Image of the power meter showing rise, overshoot, fall, and steady state

After the AXTS shutter was opened, the 2936-C power meter was allowed to read

for 10 s. Previous experimentation showed that the response typically reached steady

state around 8 s after initial exposure. The measured power was then averaged over the next 10 s. Following this procedure, it was found that the power output closely matched that measured by (Bauer, 2010), 44.8 W/cm^2.

Unable to identify the cause of the temperature response discrepancy, but recognizing that a higher temperature than was being observed would have to be experienced during an actual nuclear thermal pulse to cause a detectable change in the automobile paint, the AXTS setup was modified. Power output of the AXTS was measured with different lens configurations using the same 200 mm lens used by (Kale, 2009) and replacing the 150 mm lens used by (Bauer, 2010) with a 67.5 mm lens. Measurements were taken with various lens configurations before the final configuration, shown in Figure 18, was selected. A drawing showing the lens spacing is provided in Figure 17.
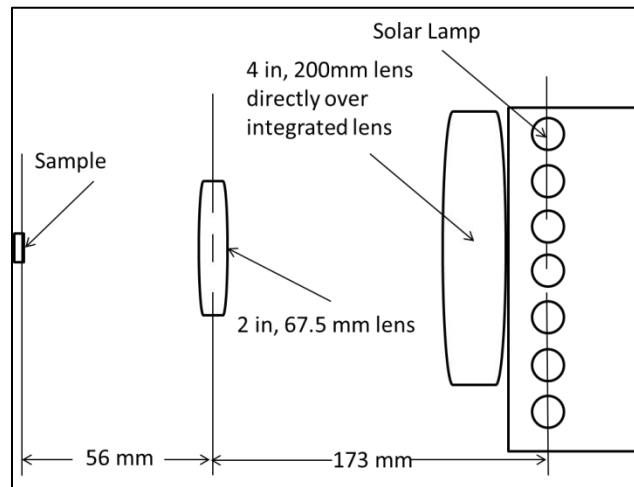
Figure 17. AXTS Setup schematic

These distances are measured from the sample surface and the lens centers. In the case of the integrated lens on the solar simulator (which cannot be seen because of the 200 mm lens sitting directly over it), it was difficult to determine the location of the lens' center. The distance recorded in the drawing is from the center-line of the cooling holes on the side of the solar simulator. Pictures of the final AXTS setup are shown in Figure 18.
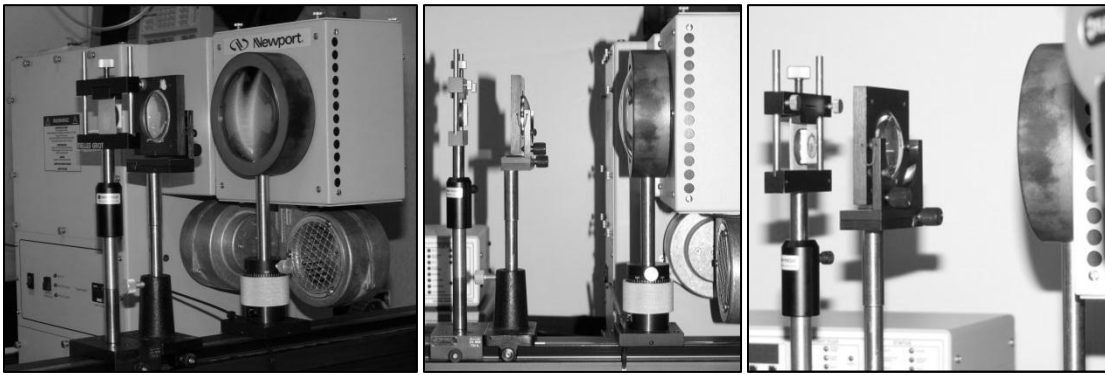
Figure 18. Final AXTS lens configuration

Because the AXTS optics had been rearranged, it was necessary to re-characterize the power distribution of the beam. While all the experiments were performed at the 1800W setting, most of the characterization work was performed at the 800W setting of the AXTS to prevent over-exposing the detector. The relationship between radiant power on the sample and AXTS power setting was linear, and, with the lenses positioned as described and the detector in place of the sample, could be described by

$$P_R = 0.035 P_A - 4.96,$$

where P_R is the measured radiant power in W/cm^2 and P_A is the power setting on the AXTS in W.

A number of knife edge tests were performed to determine the beam profile. A knife edge test consists of covering the detector with a "knife" and measuring the power detected as the "knife" uncovers the detector, slowly exposing it to light. For this research, the knife was lowered 0.1 mm each step as the detector was uncovered. The power measured at each step can be subtracted from the next measurement to determine the total power in the area that was uncovered during that step. Figure 19 shows the power measured in each step, normalized to the maximum power measured, of one of the knife edge tests as dots and a model used to describe the profile, as a solid line.
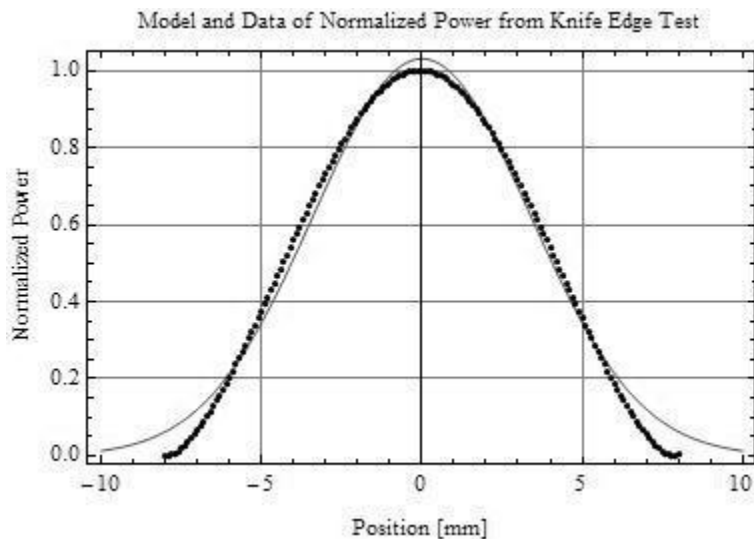
Figure 19. Normalized 1-dimensional power distribution of the AXTS

Because the steps of the knife edge test only describe the total power passing through the approximately rectangular area uncovered in each step, no information about the profile of the power perpendicular to the knife edge is provided. This information is determined by repeating the test in a direction perpendicular to the original test. In this case, the power profile was essentially the same in both directions. A revolution of the

curve shown in Figure 20 about the y-axis describes the power profile produced by the

AXTS at 800W as assembled for this research.
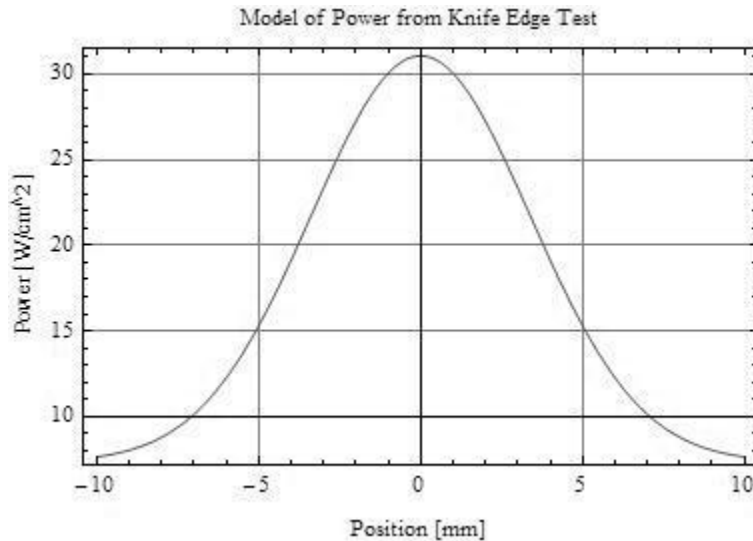
Figure 20. Modeled AXTS profile

3.3.4 Indentations

Each sample was indented 25 times in a 5x5 grid with spacing between each point

of 300, 600, or 1200 μm. Which spacing was used was determined by whether the

sample was to be measured in the center (300 μm), across the majority of the sample

(1200 μm), or a larger central region (600 μm).

From initial indentations it had been assumed that performing a pre-irradiation

measurement of each sample would be unnecessary. However, the variation in the

unirradiated samples, as much as a 25% difference in means in one case, was such that

pre-irradiation indentations became standard.

There were also changes in the depth of indentation. Initially an indentation depth

of 2000 nm was selected. It was assumed that the majority of the property changes

caused by the irradiation would be near the surface. Unfortunately, surface effects are complicated, difficult to take into account, and are the source of a great deal of variability. In order to avoid the variability caused by surface effects but still stay close to the surface, the region from 800 to 900 nm was selected for taking the measurement of modulus.

After a number of experiments, the results indicated that there was no significant difference between irradiated and unirradiated samples at that depth. There appeared, however, to be a greater difference at the limit of the indentation, 2000 nm. To see if deeper indentation would expose greater differences between pre-irradiation and post-irradiation measures, indentations were made to the load limit of the indenter, typically around 15 µm for pre-irradiated samples, and values were taken from 9 to 10 µm.

The question was raised whether multiple indentations, and thus deeper penetration, would lead to more significant differences. To answer this question, 2 indentations, each with a target depth of 10 µm below the surface, were made at each indentation location.

3.4 Finite Element Analysis Model

Because the AXTS was only capable of producing a square pulse, a method was needed for comparing the temperature response of automobile paint to the AXTS thermal pulse and the nuclear weapon shaped thermal pulse. Previous work matched total deposited energy and total pulse duration, as defined by ten times the rise time of the thermal pulse (Bauer, 2010). In order to determine the validity of this method a model was created for finite element analysis (FEA). Specific details about this model are listed in Appendix E. Finite Element Analysis Paint Model Specifications. This paint model

was then subjected to simulated thermal pulses and simulated square pulses of differing shapes, and the temperature responses were compared.

FEA was used to determine the solution of the heat transfer problem with the multi-material paint sample. For simulating the nuclear pulse, the front surface of the sample was allowed to lose heat through the free convection of the ambient air as well as radiation to the surroundings at ambient temperature. The back surface lost heat through radiation to the surroundings at ambient and internal free convection between parallel plates 3 cm apart which was selected to simulate the close proximity of auto body components to other internal vehicle components. When simulating the experimental setup, the rear surface of the sample was insulated. For both situations, the side edges of the sample were insulated and the incoming energy profile was uniformly distributed across the surface of the sample. The scenario being simulated allowed for the treatment of the problem as 1-dimensional. Any small portion of an automobile body subject to the thermal pulse of a nuclear weapon will receive a fairly uniform flux of energy incident upon it. Because of this, the only heat transfer within the body panel will be in the direction parallel to the incoming energy, and therefore, 1-dimensional. By way of example, Figure 21 shows an early attempt at comparing the modeled temperature responses to a set of normalized power profiles.

The nuclear thermal pulse was modeled with the expression

$$P(\tau) = P_0 \left(\frac{2\tau^2}{1+\tau^4} \right),$$

where P is the power, P_0 is the peak power of the pulse, $\tau = t / t_{max}$, and t is the time from the detonation of the weapon.

$$t_{max} = 41.93 \times yield^{0.464}$$

was used to solve for t_{max} (Northrup, 1996).
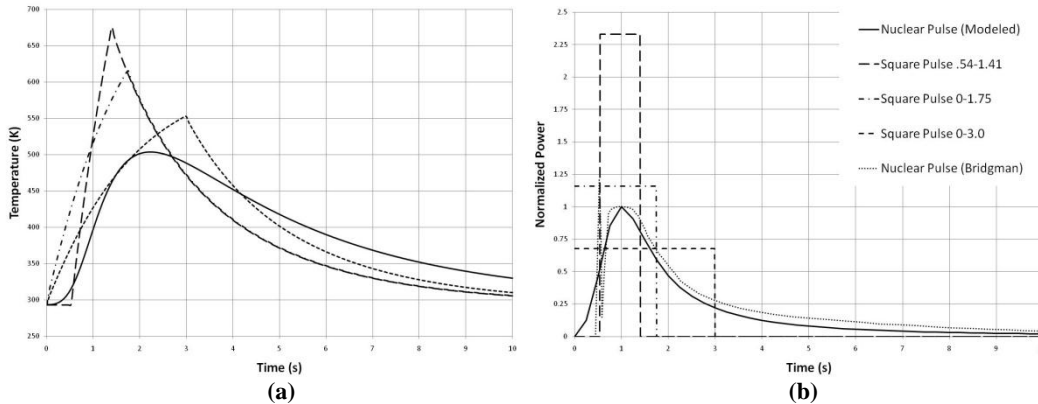
Figure 21. Comparison of the expected temperature (a) and normalized power (b) from modeled square and a nuclear pulse

Based on the measured values of the AXTS power output, all square pulse simulations were run at both 63.7 W/cm^2, the average radiant power experienced by the sample, and 81.8 W/cm^2, the peak power experience at the center of the beam. The nuclear pulse shaped simulations were run with radiant power densities of 60, 90, and 120 W/cm^2.

3.5 Assumptions and Limitations

This experimental simulation is subject to a number of assumptions and limitations in its applicability. The first limitation is that the whole experiment was performed in a laboratory environment while the situation being simulated would not resemble a laboratory environment. Specific differences include the use of well controlled, pristine paint samples, the lack of substantial atmosphere between source and sample, the ability to pre-characterize the sample, etc.

The following are the assumptions that have been made in the simulation. The weapon is only a few feet off the ground and is not below the ground at the time of detonation. The vehicle surface from which the sample is taken is perpendicular to the incoming thermal pulse, and there is a direct line of sight with no obstructions between the weapon and the vehicle. The later blast wind and associated flying debris do not damage the vehicle beyond where this process can be used and do not move the vehicle.

IV. Results

This chapter will provide a description of the results obtained and the method of conditioning the results for analysis. It will address the change in paint morphology, the change in paint properties, and the FEA modeling.

4.1 Changes in Morphology

An effort was made to correlate the steps of morphological degradation of the paint with the temperature at which the change takes place. This consisted of comparing the maximum temperature measured during the irradiation with the surface features of the sample. The maximum temperature of each sample was determined by reviewing the thermal camera video output frame by frame. The features present on the sample were identified by visual examination both with and without microscopes.

Morphological changes that were watched for included changes to the pre-irradiation indentations, sources of mass loss, such as pits or divots, evidence of changes of state of the clearcoat, and other features that were not present prior to irradiation, including bubbles, color changes, and significant changes in texture.

4.2 Changes in Properties

The nano indenter records 4 measured values, displacement into surface, load on sample, time on sample, and phase difference for each acquisition cycle. A typical indentation consists of between 2000 and 3000 acquisitions taken every 0.2 s. From these 4 measured values, harmonic stiffness, modulus, and hardness are calculated. Data files exported from the nano indenter contain all of these data in columns except phase difference.

Before the data files were generated, spurious indentation measurements were excluded from the export. These measurements were either self-identified or identified by visual inspection. The first class of spurious measures are those for which no data was recorded. These are points where the indenter failed to make an indentation in the sample. The second class are those where the machine made an indentation but was unable to identify the surface and for that reason failed to begin recording the data. Both of these two classes are self-identifying in that the export files for these indentations are blank. The third class are those indentations where the indenter made an indentation and the data was recorded, but the indentation was obviously anomalous. Examples of this third class are presented in Figure 22. Three spurious indentations present in this file, one far above and two below, have a clearly different shape from the tightly grouped indentations. In pre-irradiated samples, the cause of these spurious indentations is unknown but assumed to be imperfections in the clearcoat. Samples that attained sufficiently high temperatures during irradiation to produce surface damage also exhibited spurious indentations. These were excluded from analysis, though it was often possible to identify the source of the abnormal curves as bubbles or burned clearcoat.
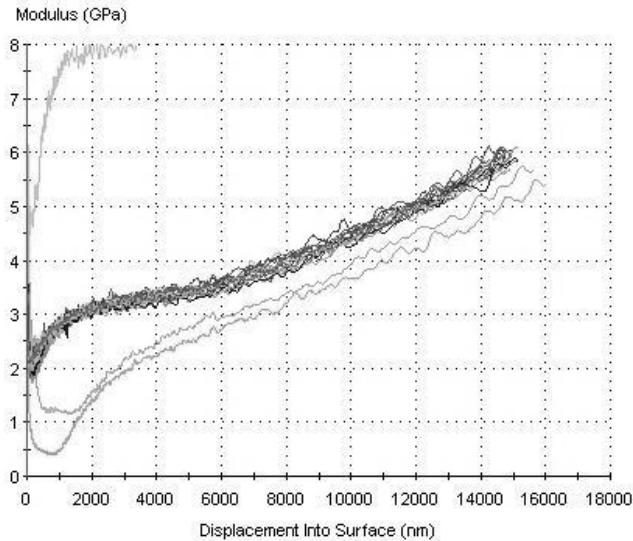
Figure 22. Typical output graph of the G200 showing three spurious indentations

After the spurious indentation measurements were removed, two general procedures were followed. These two procedures are described in the following sections along with the different techniques that used each type of data.

4.2.1 Regional Averaging

The first procedure used for extracting information from the nano indenter output data consisted of averaging the property measures between two depths. As described earlier, these depths were initially 800 to 900 nm, and were later changed to 10 to 11 µm , and ultimately to 9 to 10 µm . The data from the double-indentation samples were averaged in a region from 6 to 7 µm because the second indentations typically did not penetrate much more than 7 µm.

The initial analysis consisted of performing a Tukey-Kramer Honestly Significant Difference test of the measured moduli to determine if a statistically significant difference existed between paint samples exposed to different pulse durations. This was

done with the idea that if a statistically significant difference did exist, then perhaps a

correlation between change in modulus and yield could be determined. Figure 23

reproduces the output of the software used to perform the analysis. The low p-values

associated with each of the different level comparisons indicate a statistically significant

difference between each of the groups.

Level		Mean		Level	- Level	Difference	Std Err Dif	Lower CL	Upper CL	p-Value	
3	A	6.7948421		3	3.125	0.7391754	0.0434841	0.6252477	0.8531032	<.0001*	
2.4	B	6.6321818		2.4	3.125	0.5765152	0.0417966	0.4670087	0.6860216	<.0001*	
3.25	C	6.4367600		3.25	3.125	0.3810933	0.0404670	0.2750704	0.4871163	<.0001*	
3.125	D	6.0556667		3	3.25	0.3580821	0.0430981	0.2451657	0.4709985	<.0001*	
Levels not connected by same letter are significantly different.				2.4	3.25	0.1954218	0.0413949	0.0869679	0.3038757	<.0001*	
				3	2.4	0.1626603	0.0443489	0.0464669	0.2788537	0.0024*	

Figure 23. Results of a Tukey-Kramer Honestly Significant Difference test on the moduli of paint samples exposed to 4 different simulated thermal pulses

In order to reduce the confounding effect of the variability in pre-irradiation

measurements, the average of the 25 pre-irradiation indentations was subtracted from

each post-irradiation indentation measurement for each sample. By doing so, the change

caused by the irradiation was isolated.

4.2.2 Curve Fitting

Further examination of the nano indenter output suggested looking at the shape of the entire depth data in addition to the averaged region. By evaluating the shape of the output curves, the load and harmonic stiffness measurements produced by the nano indenter could also be evaluated. Each of the measurements produced by the nano indenter were plotted against displacement from 200 to 10,000 nm into the surface and a 3rd order polynomial was fit to the resulting curve using the method
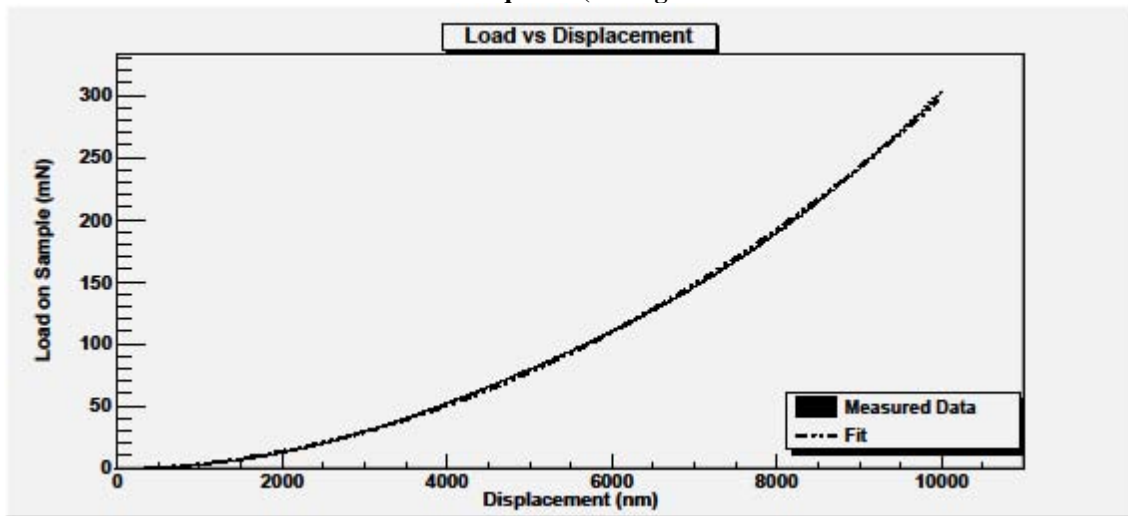
Figure 24).
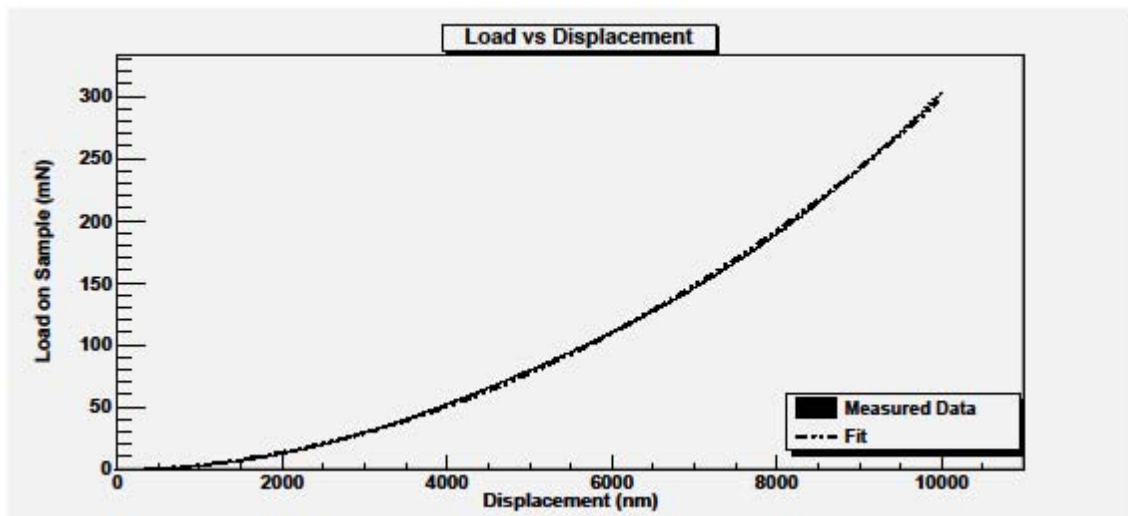
Figure 24. Measured load vs. displacement plotted with 3rd order polynomial fit

The 4 parameters of the polynomial were adjusted in the same manner as the averaged regions: to get the change resulting from the irradiation, the average of the pre-irradiated sample parameter was subtracted from the post-irradiation parameter. These changes in parameters were plotted against irradiation time and the degree of correlation was determined.

4.3 FEA Modeling

   The FEA results consisted of temperatures measured at different time intervals. The temperature was measured 1 µm into the clearcoat. A comparison was made between the temperature response predicted by the simulation and those measured during the irradiation experiments. Figure 25 shows some of these results in the form of a comparison between the maximum temperatures measured during irradiation experiments and the maximum predicted for those same exposure times.
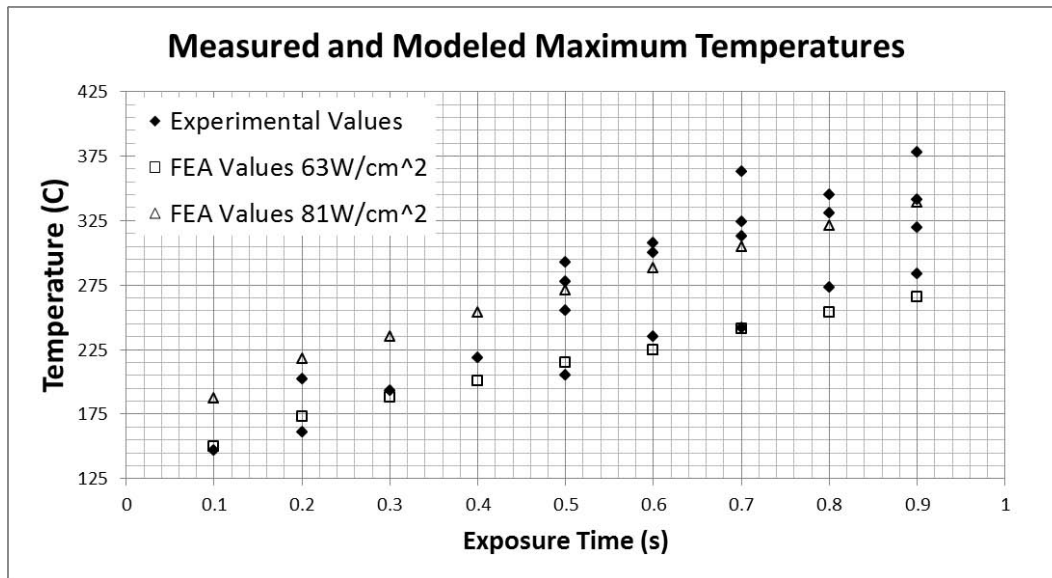
Figure 25. FEA predicted and experimentally measured maximum temperatures at different exposure times

   From each simulation, the maximum temperature attained was identified and the amount of time the measured temperature was above 50% of this maximum temperature was determined. These two values, the maximum temperature and time above 50% of maximum were used to compare square pulses to nuclear shaped pulses.

<div align="center">**V. Analysis**</div>

5.1 Morphology of Thermal Degradation of Automobile Paint

Clearcoat "recovers" from indentation upon heating at temperatures as low as 106°C. Figure 26 presents two images that demonstrate the tendency of the clear coat to recover. A scratch present on a sample is shown prior to irradiation on the left and the same scratch is shown after a 0.64 s irradiation on the right. The reduction in the width of the scratch is evident, as is the reduction in the size of the small imperfections in the surrounding clearcoat. That the post-irradiation scratch's surface does not appear smooth, but, in fact, seems to have more features than the pre-irradiation scratch suggests that the clearcoat does not become liquid and flow during this process. Instead, it seems, the clearcoat relaxes and returns to a pre-deformed configuration. This conclusion is based on the assumption that the surface tension of a liquid clearcoat would form a smooth surface which would remain after re-solidification.
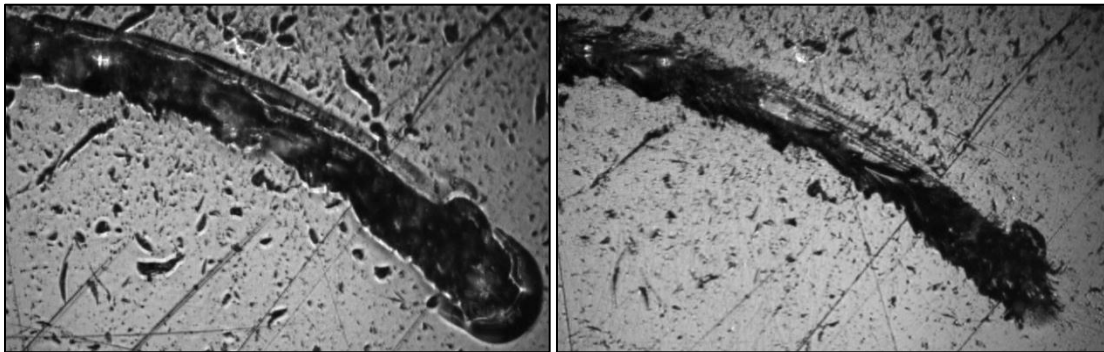
Figure 26. A scratch pictured before (left) and after (right) a 0.64 s irradiation

(Bauer, 2010) suggested a number of chemical mechanisms by which the various polymer chains within paint systems sustain thermal degradation. This research

continues the examination of degradation mechanisms by identifying a series of

morphological steps by which this degradation occurs. Figure 27 presents a paint sample

that shows these steps from the left side of the image to the right. As the temperature of

the paint sample rises, the layers below the surface begin to release volatiles. These

volatiles are trapped by the clearcoat top layer. The rising temperature causes the

clearcoat to soften and, as the volatiles coalesce, the pressure from the volatiles forms

bubbles within the clearcoat. These bubbles vent their contents shortly after being

formed. The raised clearcoat then begins to degrade, first turns white, and, then, darkens

and begins to burn. The minimum temperatures at which these steps were observed to

occur are recorded in Table 1. There are two values recorded in the bubble and

whitening rows under the Highest Temperature not Observed because the experiment that

yielded the temperature of 363°C was anomalous in that it produced the second highest

temperature at an exposure of only 0.7 s and insignificant morphological changes. Note

in Figure 25 that this data point does not fall on the same line as the other observations

do. The other values in the table are the next highest temperature observed where the

samples do not show the listed morphological behavior.
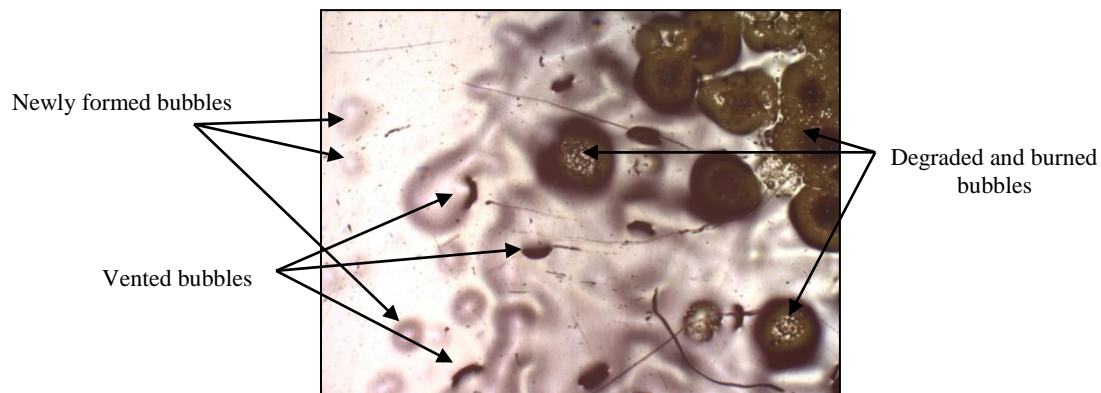
Figure 27. Paint sample showing stages of thermal degradation

Table 1. Observed morphological changes in clearcoat and corresponding temperatures in degrees Celsius

Behavior	Lowest Temperature Observed	Highest Temperature not Observed
Recover	106	Observed in every test
Bubble	284	363, 313
Whitening	331	363, 345

Figure 28 shows the next steps in this degradation where the clearcoat has burned away, exposing the lower layers. It is plausible that at this point in the degradation process the paint sample generates a flame, though that this is the exact point at which a flame appears has not been conclusively demonstrated. It appears that the lower layers delaminate from the steel substrate, as in Figure 28, which action has the compounding effect of reducing the heat transferred away from the paint and into the steel. This causes a spike in the temperature and the assumed formation of a flame. The flame burns the delaminated material, adding heat to the surrounding paint and consuming it as it, too, delaminates from the substrate.
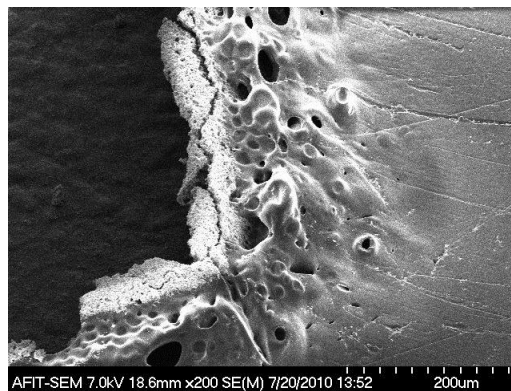
Figure 28. SEM image of a burned paint sample showing the effects of delamination

5.2 Paint Properties Affected by a Thermal Pulse

5.2.1 Regional Averaging

Changes in properties from 800 to 900 nm below the surface show almost no correlation with exposure time, as established earlier. Average values of elastic modulus and hardness in the 9-10 µm depth show a weak correlation with exposure time.

Figure 29. Change in elastic modulus against exposure time with fit line and a shaded 95% confidence interval for 9-10 µm indentation averages

Figure 29 is a plot of the change in elastic modulus against exposure time with a linear fit and a shaded 95% confidence interval. The correlation between change in elastic modulus and exposure time, as described by the linear fit line is given by the relationship,

$$\Delta M = -0.365 + 0.867t,$$

where ΔM is the change in elastic modulus, and *t* is the duration of irradiation. The

degree of goodness of fit of this relationship to the collected data is given by an R^2 value

of 0.440.

The data taken from samples exposed for 0.87, 0.89 and 0.9 s had begun to

degrade and had bubbling on the surface. Figure 30 is a reproduction of Figure 29

without the data from those samples. While the removal of those points decreases the

width of the confidence interval, the overall effect is also to lower the R^2 value to 0.327.

The function describing this relationship is

$$\Delta M = -0.273 + 0.590t$$.

Figure 30. Change in elastic modulus against exposure time with fit line and a shaded 95% confidence interval for 9-10 μm indentation averages without bubbling sample data

As an example of the utility of these relationships, if a modulus difference

between the exposed side of a car and the unexposed side is 0.2 GPa, the second model

predicts with 95% certainty that the corresponding exposure time is between

approximately 0.20 and 1.45 s, which correspond to a weapon size approximately

between 5 and 62 kT. The width of these confidence intervals is largely a result of the

variability in the modulus in each sample. This variability remained essentially the same

after irradiation as it was before. The standard deviation of the elastic modulus for all

samples prior to irradiation was 0.2756 GPa for a mean of 4.5987 GPa. In individual

samples, the average standard deviation was 0.0912 GPa before irradiation and 0.0942

after.

      Average values measured between 6 and 7 μm of the second indentation, which

correspond to roughly 12 to 13 μm below the surface of the sample, similarly show a

weak correlation with exposure time. The plot of this data is contained in Figure 31. The

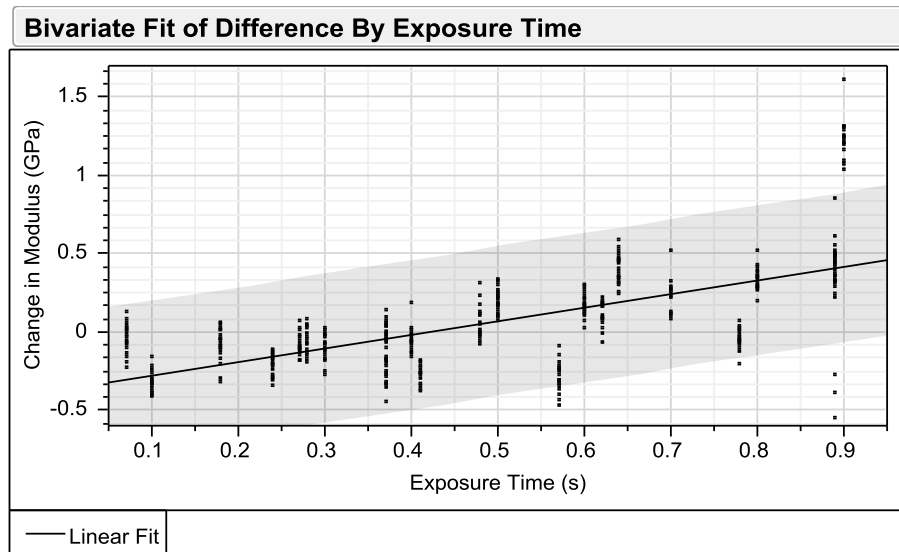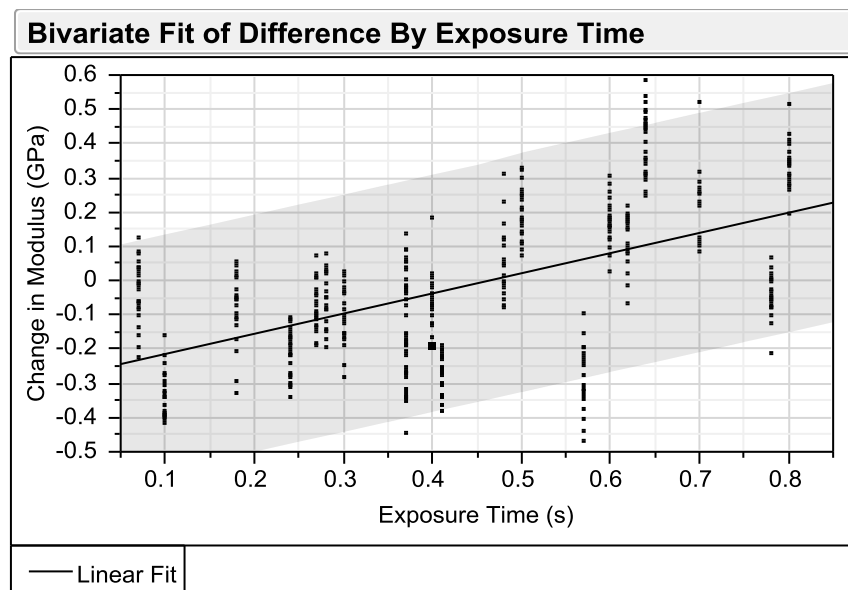R^2 value for this fit is 0.1853, and, as is shown, the 95% confidence interval is very wide.
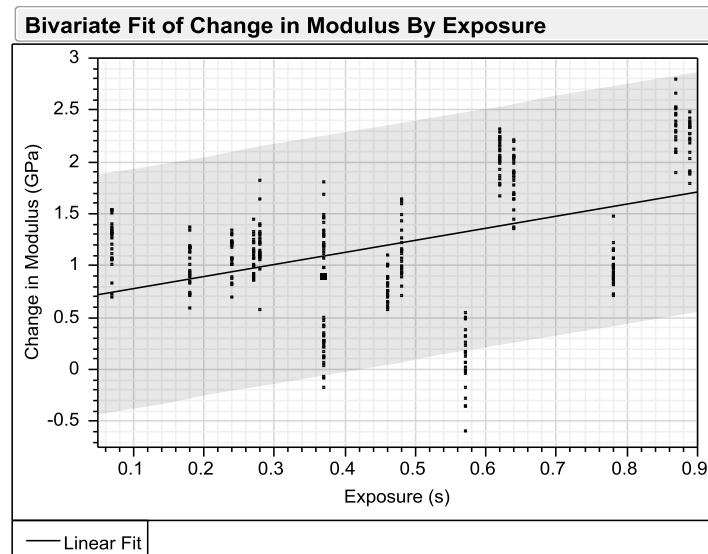
Figure 31. Change in elastic modulus against exposure time with fit line and a shaded 95% confidence interval for 6-7 μm indentation averages of second indentation

5.2.2 Curve Fitting

The correlation between the parameters determined by curve fitting is similarly weak. Figure 32 shows the strongest of the correlations, the 3rd parameter of the fit for harmonic stiffness plotted against displacement into surface by exposure time. The R^2 value for this correlation is 0.5773.
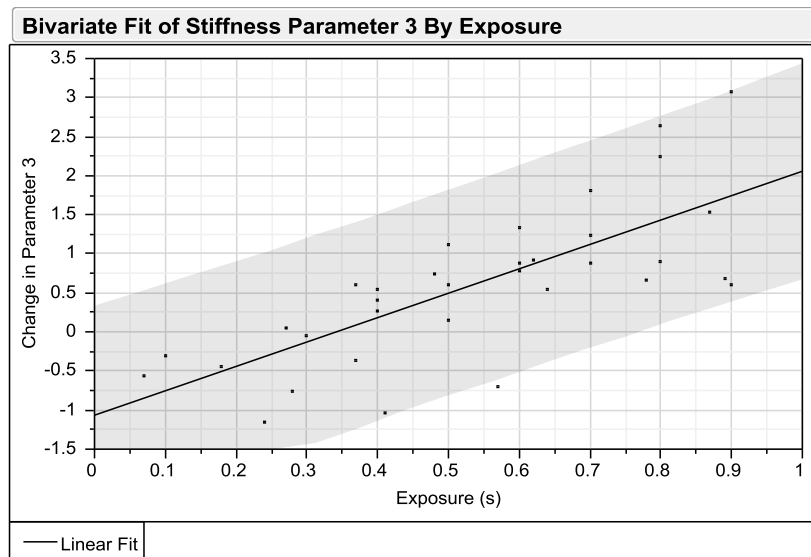
Figure 32. Change in harmonic stiffness parameter 3 vs. exposure time with linear fit and a shaded 95% confidence interval

Table 2 shows the correlation for each of the parameters and each of the recorded properties. The coefficients were determined using the residual or restricted maximum likelihood method which provides the general strength of the linear correlation. It is the equivalent of an R value for a linear fit to the same data.

The correlations for the multiple indentation parameters were not significantly higher than those with single indentations. Table 3 provides these coefficients.

Table 2. Correlation coefficients of single indentation curve fitting parameters

Correlation Coefficients of Single Indentation Samples				
	Parameter 1	Parameter 2	Parameter 3	Parameter 4
Hardness	0.1518	-0.1658	0.1799	0.2312
Load on Sample	0.6323	0.3186	0.2183	-0.0642
Modulus	0.036	-0.0342	0.0937	0.3068
Harmonic Stiffness	0.1137	0.4636	0.7917	0.0307

Table 3. Correlation coefficients of second indentation curve fitting parameters

Correlation Coefficients of Double Indentation Samples				
	Parameter 1	Parameter 2	Parameter 3	Parameter 4
Hardness	0.4089	0.3695	0.2228	-0.1432
Load on Sample	-0.2447	0.3719	0.1459	-0.4615
Modulus	0.1535	-0.1622	0.1702	0.1497
Harmonic Stiffness	-0.1187	0.1053	0.2882	-0.1275

5.3 Simulating a Nuclear Pulse

The FEA model temperature response was compared with the sample temperature response observed during experiments in order to validate the model. A comparison of the two indicates an acceptable match. Figure 33 shows two modeled square pulses along with four experimentally measured temperature responses to a 0.9 s pulse from the AXTS. These results indicate that the model does reasonably well at approximating the rise of the temperature, but is less accurate in predicting the temperature decay after the pulse has ended.

A number of attempts were made to capture this slow temperature decay in the model. Incorporation of the sample holder insulating foam into the model had no effect on the decay rate. Adjustments to the free convection and radiant losses similarly had very little effect on the decay rate. This last piece of information indicated that the slow

decay was not a result of reduced losses to the ambient atmosphere, but was, in fact, something hindering the energy in the paint from diffusing into the substrate.

It was hypothesized that the formation of volatiles and their coalescing into bubbles was the source of the slow temperature decay rate. This was modeled by placing spheres of air 0.1 to 1 µm in diameter in the basecoat layer of the model at intervals of 0.5 µm along the entire length of the sample. These inclusions had very little effect on the temperature response of the model.
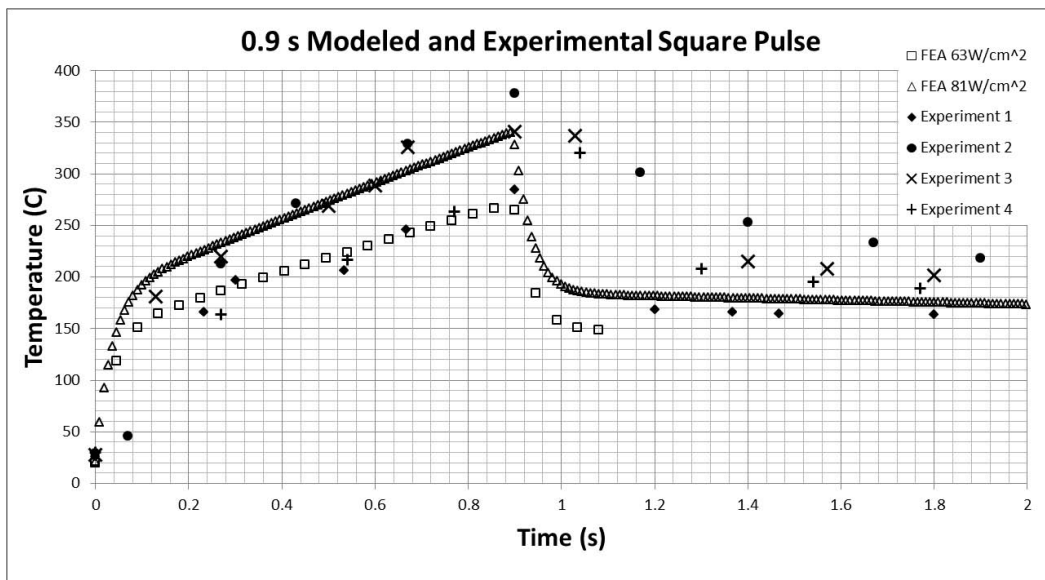
Figure 33. 0.9 s exposure modeled and experimental temperature response

In comparing the modeled square pulse to the modeled nuclear pulse, it was decided that matching the maximum temperature attained and the amount of time spent above half of the maximum temperature would be a reasonable method for comparing the AXTS thermal pulses to nuclear weapon pulses. Each exposure time used in the experiments was modeled at both 63 and 81 W/cm^2. By using these two fluxes, ranges of

maximum temperatures and times above half maximum were established for each

exposure time. Matching the maximum temperature and time above half maximum

temperature can be thought of as matching the yield of the weapon and the distance from

ground zero at which it is measured. The yield controls the duration of the pulse and the

distance controls its intensity. Because two maximum temperatures and two times above

half maximum temperature were created for each exposure time, an infinite number of

yield and range combinations could be found which have maximum temperature and time

above half maximum between those found for the square pulse.

Table 4. Ranges of maximum temperature and time above half maximum temperature for square pulses along with matching nuclear thermal pulse characteristics

Exposure Time	63W/cm^2		81W/cm^2		Nuclear Thermal Pulse Characteristics					
	Max Temp (C)	Time (s)	Max Temp (C)	Time (s)	Yield (kT)	Flux (W/cm^2)	Distance (km)	Max Temp (C)	Time (s)	Min Dist (km)
0.1	150	0.120	188	0.118	0.5	120	0.504	153	0.118	0.325
0.2	173	0.220	218	0.216	4	93	1.025	184	0.215	0.651
0.3	188	0.330	235	0.321	10	90	1.346	197	0.329	0.883
0.4	201	0.440	254	0.420	15	90	1.508	205	0.427	1.01
0.5	215	0.550	271	0.530	20	97	1.575	223	0.531	1.11
0.6	228	0.660	288	0.648	25	111	1.567	258	0.652	1.20
0.7	241	0.800	305	0.777	30	112	1.642	263	0.800	1.27
0.8	254	0.920	322	1.368	35	120	1.656	284	1.00	1.34
0.9	266	1.000	339	2.241	40	120	1.719	288	1.23	1.40

Table 4 contains the results from the modeled square pulses along with the

characteristics of a nuclear thermal pulse that corresponds with a given AXTS exposure.

In addition to the nuclear thermal pulse weapon yield, Yield, maximum temperature, Max

Temp, and time above half maximum, Time, the table also lists the flux used to model a

weapon of that yield, the distance from ground zero at which such a flux would be experienced, Distance, and the minimum forensic distance, Min Dist, as established by (Bauer, 2010) for a weapon of the given yield. The weapon characteristics for the 0.5, 0.6, and 0.7 s exposure times were determined by interpolating between the results of their corresponding weapons modeled at 90 and 120 W/cm^2. Figure 34 shows an example of the temperature response to a nuclear weapon thermal pulse and two modeled square pulses as well as one experimentally measured temperature response.
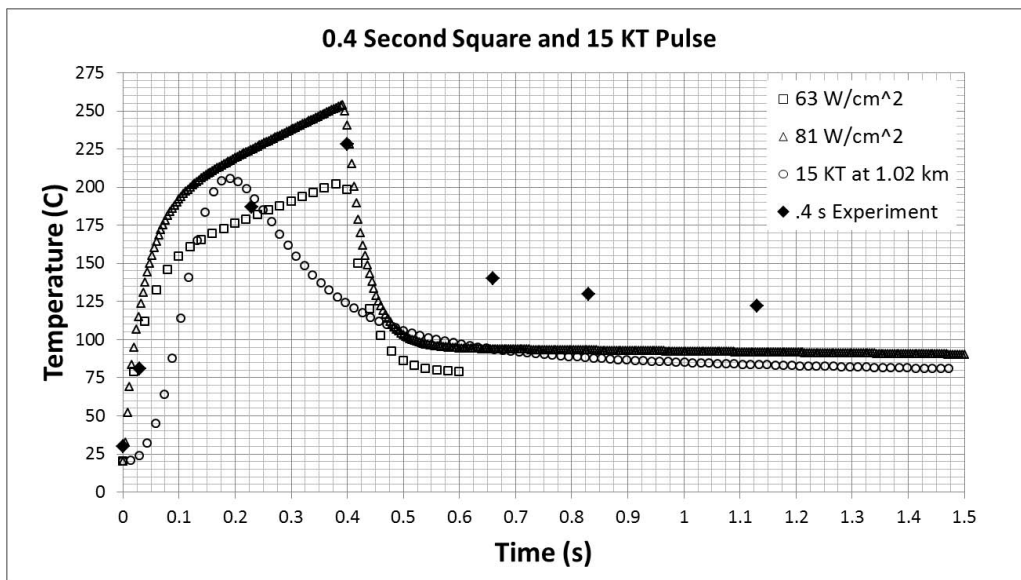

Figure 34. Modeled and experimental 0.4 s pulse and 15 kT weapon at 1.02 km

VI. Conclusion

The hypothesis with which this research began was:

Differences between the elastic modulus, as measured by nano indentation, of automobile paint samples subject to thermal irradiation from a simulated nuclear weapon and unirradiated samples will exist such that a model relating those differences to the power and duration of exposure can be developed.

From the results obtained and the analysis provided, it seems apparent that this hypothesis, at least as tested here, is not correct. While it is true that a model relating the two has been developed, the weak correlation and wide confidence intervals, due in part to the variability both before and after irradiation, suggest that the model could not be used for forensics. Going beyond the use of elastic modulus described in the hypothesis, this research has also demonstrated that the hardness and harmonic stiffness of automobile paint, and the nano indenter's load on sample required to achieve a given depth are all similarly of little value in retroactively determining the yield of a nuclear weapon.

However, this research did not test the entirety of the stated hypothesis; rather, it tested a hypothesis which says that the yield of a nuclear weapon can be determined from nano indentation measurements of the clearcoat layer of automobile paint. The hypothesis, stated in this manner, has been demonstrated to be false. This leaves the door open to the possibility that nano indentation of, perhaps, the basecoat, after the removal of the clearcoat, would be able to provide the sought after correlation.

Understanding the morphological changes that occur as automobile paint degrades also has the possibility of being useful for forensics. By determining if a strong

correlation between some useful parameter, such as temperature, exposure time, weapon yield, etc., and the morphological changes exist, a more sensitive metric for determining yield might become apparent. One possibility would be to use a microscope to examine the "topographical" features of the paint sample pre and post-irradiation and quantify the changes that occur. Potential quantities that could be used are the number density of bubbles, the degree of whitening or other color changes, or the average reduction in size of imperfections due to the clearcoat recovering.

There are a number of other topics future research could pursue as follow-on to this project. These include investigating the cause of the variability in the unirradiated paint properties, investigating other layers of paint, and considering the sensitivity of the viscoelastic properties of the clearcoat to the thermal pulse. Another path to pursue is investigating changes in the chemical properties of the paint caused by the thermal pulse. In addition to seeking greater understanding of the paint, modifying the AXTS to provide a pulse shape that more closely resembles an actual nuclear pulse would enhance its research utility. Until this is done, and perhaps even after, working with the computer model developed for this research presents another avenue for research. The mechanism that causes the samples' slow temperature decay after irradiation still needs to be identified and incorporated into the model.

As a final recommendation for any follow on research, a minor change in approach from that followed here and in previous research might prove beneficial. Keeping in perspective that the goal is the identification of a method for accurately and rapidly determining the yield of a nuclear weapon after detonation, it stands to reason that simply examining changes due to AXTS pulses of different lengths but constant power is

logically begging the question—assuming the answer from the beginning. It is, essentially, assuming that the sample collector knows at what distance from the weapon the sample experienced a flux equivalent to that produced by the AXTS. However, the only way the operator could have known this is if he knew the yield of the weapon, which is why he is collecting the sample. A better approach might be to select a set distance from ground zero and modify the AXTS settings to match multiple parameters of specific weapons (e.g. flux, time of exposure, pulse shape).

With better understanding of the morphological response of the paint to the thermal pulse, another option might present itself. This research seems to suggest that there are distinctive temperature bands in which certain morphological changes take place in the clearcoat. By assuming instructions to the sample collectors to bring in the sample furthest from ground zero that exhibits a certain morphological feature, then the knowledge of the distance at which the sample was collected could provide a good starting estimate of the yield. This narrowed space of weapon yield could then be further decreased by using a more precise method, such as quantitatively examining the morphological features or using any of the other suggested techniques. With this in mind, the experimenter's goal would be to find the correct distance and yield that produce the specific morphological feature. Developing a research approach from either of these starting points makes better sense with regard to the application technology. This research, and that which precedes it, should provide a useful springboard from which to start.

Appendix A. Agilent Nano Indenter G200 Specifications

Agilent Nano Indenter G200 Specifications

Standard XP Indentation Head	
Displacement resolution	<0.01 nm
Total indenter travel	1.5 mm
Maximum indentation depth	>500 μm
Load application	Coil / magnet assembly
Displacement measurement	Capacitance gauge
Loading capability	
Maximum load (standard)	500 mN
Maximum load with DCM II option	30 mN
Maximum load with High Load option	10 N
Load resolution	50 nN
Contact force	<1.0 μN
Load frame stiffness	~5 x 106 N/m
Indentation placement	
Useable surface area	100 mm x 100 mm
Position control	Automated remote with mouse
Positioning accuracy	1 μm
Microscope	
Video screen	25x (x objective mag.)
Objective	10x and 40x

Appendix B. FLIR PM695 Specifications

Specification	Value
Field of View / Min focus distance	24°x18° / 0.5m
Spatial resolution (IFOV)	1.3 mrad
Thermal Sensitivity	0.08°C at 30°C
Image Frequency	50 / 60 Hz non-interlaced
Detector Type	Focal Plane Array (FPA), uncooled microbolometer 320 x 240 pixels
Spectral Range	7.5 to 13µm
Temperature Range 1 Temperature Range 2 Temperature Range 3	-40°C to 120°C 0 to 500°C 350°C to 2000°C
Accuracy	±2°C
Operating Temperature Range	-15°C to +50°C
Storage Temperature Range	-40°C to +70°C
Weight	2.4 kg (5.3lbs.), including battery
Size	209mm x 122mm x 130mm (8.23" x 4.80" x 5.12")

Appendix C. Newport 818P-030-18HP Thermopile Specifications

Certificate #:   181210-090406   Customer Name:
Model Number: 818P-030-18HP   V5   Instrument ID:
Serial Number: 181210   Date of Calibration: Jan. 23, 2009
Cal. Procedure: 420- 19325   Calibration Due Date: *

Calibration Data

				Power Level					
λ	Sensitivity		Into Load	Power	Rep.Rate	Ambient Temp.	Relative humidity	0-95% Risetime	Beam Ø @ 1/e^2
μm	mV/W	%	Ω	Watts	Hz	°C	%	s	mm
1.064	P 0.3601	± 2.5	100K	15	cw	23	20	2.6	13.6

S Value Corrected According To Spectral Absorption Curve
P Sensitivity programmed in detector head
Note: For legacy power meter models which do not have the direct capability to read EEPROM, you can adjust the power with :

λ_1:   Wavelength listed above
λ_2:   The new wavelenth

P(λ_1): Measured Power   P(λ_2): Power adjusted for new wavelength
S(λ_1): Sensitivity listed above   S(λ_2): Sensitivity at new wavelength. Infer from absorption table and plot.

Detector Response
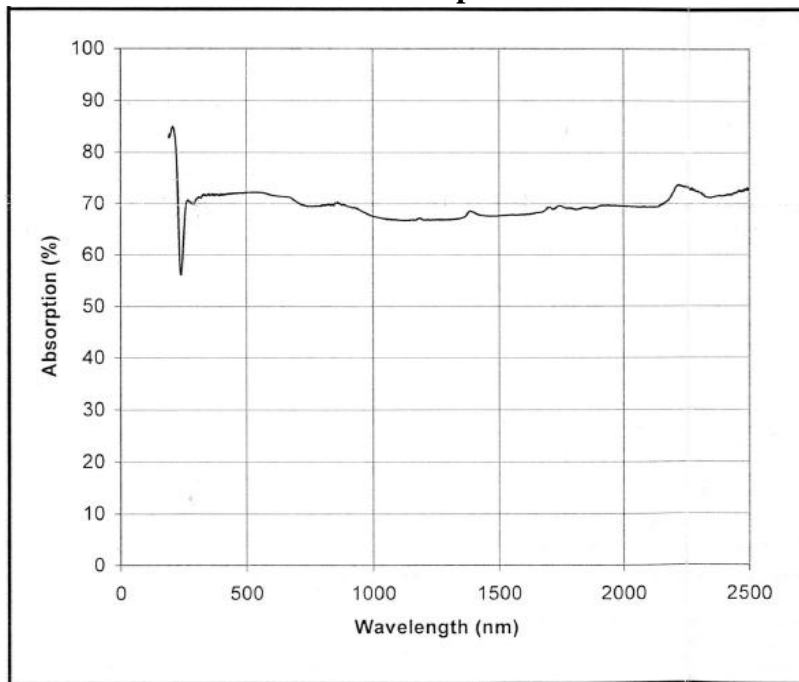
Appendix D. Newport 2936-C Parameters

Parameter	Value
Wavelength	1064 nm*
Range	2.733 W/cm^2
Range	Auto
Attenuator	Off
Analog Filter	Off
Digital Filter	Off
Units	W/cm^2
Mode	CW Cont.
Detector	818P-030-18HP
S/N	181210
Det. Temp.	No Therm.
Responsivity	3.601E-4
Ref Value	0.0010 W/cm^2
Offset	0.0000 W/cm^2
Num Digits	5
Spot Size	2.5400 cm^2

*Power meter calibrated to 1064 nm

Appendix E. Finite Element Analysis Paint Model Specifications

The paint model has the following details

Material Properties				
Layer	Thermal Conductivity	Density	Heat Capacity	Thickness
	W/(cm K)	g/ cm^3	J/(g K)	um
Clearcoat	0.0021	1.2	1.8	30
Basecoat	0.0041	1.17	1.28	15
Surfacer	0.0024	1.4	1.11	20
Electrocoat	0.0027	1.25	1.11	30
Zinc Phosphate	0.0052	4	0.13	5
Steel	0.54	7.8	0.49	850
Fiberglass	.00048	.096	0.9	3000

Bibliography

Adamsons, K. (2002). Chemical depth profiling of multi-layer automotive coating
    systems. Progress in Organic Coatings, 45(2-3), 69-81.

Bridgman, C. J. (2001). Introduction to the physics of nuclear weapons effects, Defense
    Threat Reduction Agency, pp 535.

Capper, P. & Elliot, C.T. (2001). Electronic Materials & Infrared Detectors and Emitters:
    Materials and Devices. Boston, MA. Kluwer Academic.

Fischer-Cripps, A. C. (2002) Nanoindentation, New York: Springer.

Drzal, P. L., Sung, L.P., Britz, D., & Ryntz, R. (2005) Nanomechanical properties of
    polymeric coatings through instrumented indentation. International Coatings for
    Plastics Symposium.

Koehl, Michael A. (2009) Thermal Flash Simulator MS Thesis. AFIT/GNE/ENP/09-
    M04. Wright-Patterson AFB OH: Graduate School of Engineering, Air Force
    Institute of Technology.

Lambourne, R., & Strivens, T. A. (1999). Paint and surface coatings - theory and practice
    (2nd Edition ed.) Woodhead Publishing.

Mock, Todd A. (2010) Evaluation of Material Response to Thermal Flash MS Thesis.
    Gainesville, FL University of Florida.

Newport. Oriel Product Line Stratford, CT (2008) 150W, 300W and KW large area light
    source--User Manual.

Northrop, J. A., Defense Special Weapons Agency Alexandria VA, (1996). (U)
    Handbook of nuclear weapon effects: Calculational tools abstracted from (EM-1).

Oliver, W.C., & Pharr, G.M., (2003). Measurement of hardness and elastic modulus by
    instrumented indentation: Advances in understanding and refinements to
    methodology. Materials Research, 19(1), 3-20.

Poilane C., Delobelle P., Bornier L., Mounaix P., Melique X., & Lippens D., (1999).
    Determination of the mechanical properties of thin polyimide films deposited on a
    GaAs substrate by bulging and nanoindentation tests. Materials Science and
    Engineering, A262, 101-106.

Plum, W. B., & Parker, W. J., Naval Radiological Defense Lab San Francisco California
    (1958). (U) Spectrometer Measurements.

Stachitis, Tucker (2009) Evaluation of 3-D Radiant Heat Transfer in Street Canyons MS Thesis. Gainesville, FL University of Florida.

REPORT DOCUMENTATION PAGE

1. REPORT DATE *(DD-MM-YYYY)* 24-03-2011	2. REPORT TYPE Master's Thesis	3. DATES COVERED *(From – To)* June 2009 – Mar 2011

-TITLE AND SUBTITLE Nuclear Weapon Yield Determination through Nano Indentation of Thermally Degraded Automobile Paint	5a. CONTRACT NUMBER
	5b. GRANT NUMBER
	5c. PROGRAM ELEMENT NUMBER
6. AUTHOR(S) Richards, Michael J., Captain, USAF	5d. PROJECT NUMBER N/A
	5e. TASK NUMBER
	5f. WORK UNIT NUMBER

7. PERFORMING ORGANIZATION NAMES(S) AND ADDRESS(S) Air Force Institute of Technology Graduate School of Engineering and Management (AFIT/EN) 2950 Hobson Way WPAFB OH 45433-7765	8. PERFORMING ORGANIZATION REPORT NUMBER AFIT/GNE/ENP/11-M17
9. SPONSORING/MONITORING AGENCY NAME(S) AND ADDRESS(ES) DTRA/NTD 8725 John J. Kingman Rd MS 6201 Attn: Maj Todd Ewy Ft Belvoir, VA 22060-6200	10. SPONSOR/MONITOR'S ACRONYM(S)
	11. SPONSOR/MONITOR'S REPORT NUMBER(S)

12. DISTRIBUTION/AVAILABILITY STATEMENT
APPROVED FOR PUBLIC RELEASE; DISTRIBUTION UNLIMITED

13. SUPPLEMENTARY NOTES

14. ABSTRACT
This work investigated the suitability of automotive clearcoat as a nuclear weapon yield sensor, using the change in elastic modulus as the primary metric. The AFIT Xenon Thermal Simulator (AXTS) was used to simulate a nuclear thermal pulse. The elastic modulus of the clearcoat was measured using a nano indenter. During this research the power density of the AXTS beam was increased from 44.7 to 63.7 W/cm2. The morphological steps through which automobile paint proceeds as it thermally degrades were identified and correlated with temperatures. A computer model was created and used to ensure that the paint's time-temperature response to the AXTS pulse was comparable to that of a replicate nuclear thermal pulse.

Clearcoat's physical properties exhibit a low sensitivity to incident thermal energy. Variability among these properties remains essentially unchanged by exposure to the thermal pulse. A weak correlation between change in elastic modulus and exposure time was identified. A similarly weak correlation between exposure time and each of load on sample, harmonic stiffness, and hardness was also identified. It was concluded that these correlation were too weak to be used for post-detonation forensics.

15. SUBJECT TERMS
Nuclear weapon yield, thermal flash, nano indentation

16. SECURITY CLASSIFICATION OF:			17. LIMITATION OF ABSTRACT	18. NUMBER OF PAGES	19a. NAME OF RESPONSIBLE PERSON Dr. James Petrosky (AFIT/ENP)
a. REPORT U	b. ABSTRACT U	c. THIS PAGE U	UU	71	19b. TELEPHONE NUMBER *(Include area code)* 937-785-3636 ext. 4562 james.petrosky@afit.edu